Journal of
Materials Chemistry C

Bond Valences and Anharmonicity in Vacancy-Ordered Double Perovskite Halides

Journal:	*Journal of Materials Chemistry C*
Manuscript ID	TC-ART-07-2018-003527.R2
Article Type:	Paper
Date Submitted by the Author:	16-Oct-2018
Complete List of Authors:	Maughan, Annalise; Colorado State University, Chemistry Paecklar, Arnold; Colorado State University, Chemistry Neilson, James; Colorado State University, Chemistry

SCHOLARONE™
Manuscripts

Journal Name

ARTICLE TYPE

Cite this: DOI: 10.1039/xxxxxxxxxx

Received Date
Accepted Date

DOI: 10.1039/xxxxxxxxxx

www.rsc.org/journalname

Bond Valences and Anharmonicity in Vacancy-Ordered Double Perovskite Halides[†]

Annalise E. Maughan[a], Arnold A. Paecklar[a], and James R. Neilson*[a]

Anharmonic lattice dynamics are intimately linked with optical and electronic properties in perovskite halides semiconductors. Vacancy-ordered double perovskites are a subset of the perovskite halide family containing isolated octahedral units. The absence of polyhedral connectivity engenders the vacancy-ordered double perovskites with additional degrees of dynamic freedom, which presents an ideal structural framework to study dynamic-property relationships in perovskite halide semiconductors. In the present study, we examine the structure and bonding origins of anharmonicity in the vacancy-ordered double perovskites $Cs_2Sn_{1-x}Te_xI_6$. While X-ray diffraction indicates that all members adopt the cubic vacancy-ordered double perovskite structure, the local coordination environment probed by X-ray pair distribution function (XPDF) analysis reveals asymmetry of the Cs–I/I–I pair correlation that smoothly decreases with increasing tellurium content. Temperature-dependent neutron total scattering suggests that this asymmetry in the PDF occurs due to anharmonic lattice dynamics arising from octahedral tilting and Cs^+ displacements, as supported by Reverse Monte Carlo simulations of the Cs_2SnI_6 and Cs_2TeI_6 end members. We further correlate the trends in asymmetry and anharmonicity with the bond valence sum of the Cs^+ ion, and find that the anharmonicity vanishes when the bonding preferences of the Cs^+ are satisfied by the size of the cuboctahedral void. This study presents a simple and effective approach for understanding the origin of anharmonicity in vacancy-ordered double perovskite materials.

Introduction

Lattice dynamics play a crucial role in dictating materials properties, including thermal conductivity,[1] ionic and electronic transport,[2,3] optical emission,[4,5] piezoelectricity and ferroelectricity,[6,7] and superconductivity,[8] to name a few. Divergence from a purely harmonic vibrational landscape further manifests interesting physical behavior. High amplitude anharmonic vibrations in systems such as the tin and lead chalcogenides serves to introduce vibrational disorder to which their low thermal conductivities and advantageous performance in thermoelectric devices are attributed.[9–11] Anharmonic rattling of guest atoms within host structures has been exploited as a mechanism to disrupt thermal conductivity in other candidate thermoelectric materials such as skutterudites.[12] Additionally, ionic conductivity may be enhanced in materials in which the mobile ion occupies a flat and broad anharmonic potential well,[13,14] while lower-energy anharmonic vibrational modes can couple to mobile electrons to reduce electron mobilities.[2,15] Despite the extensive influence of anharmonicity upon functional properties in crystalline materials, a unified understanding of the structural and bonding motifs necessary to leverage anharmonic behavior to target particular materials properties is fundamentally lacking.

Halide-based perovskite materials are redefining the paradigm of semiconductor materials design principles, in that they appear to follow a set of structure-dynamics-property relationships that are distinct from conventional semiconductors. The perovskite structure adopts the general formula ABX_3, and the structure is composed of corner sharing BX_6 octahedra with A-site cations in the 12-coordinate void. Anharmonic lattice dynamics in perovskite halides have been shown to arise from rotational instabilities of the soft, deformable BX_6 octahedral framework coupled with motions of the A-site cation.[16–18] These dynamic instabilities yield an anharmonic double potential well, resulting in an instantaneous local structure characterized by cooperative octahedral tilting that averages to a higher-symmetry, untilted structure.[16–19] Anharmonicity has been further correlated with the remarkable photoconversion efficiencies of halide perovskite materials in photovoltaic devices.[20,21] Of particular note is the observation of long carrier excited-state lifetimes,[22–24] which is hypothesized to arise from the formation of polarons that protect photogenerated charge carriers and prevent recom-

---

[a] Department of Chemistry, Colorado State University, Fort Collins, CO, 80523-1872 E-mail: james.neilson@colostate.edu

[†] Electronic Supplementary Information (ESI) available: Data from additional Reverse Monte Carlo simulations. See DOI: 10.1039/b000000x/

bination.[15,24–30] The intimate link between anharmonic lattice dynamics and functional properties motivates a fundamental understanding of the structural and compositional origins of anharmonicity in perovskite halides.

Vacancy-ordered double perovskites present a materials family to study anharmonicity in a lattice with additional dynamic degrees of freedom. The vacancy-ordered double perovskite structure is formed by doubling the conventional ABX_3 perovskite unit cell and removing every other B-site cation to form a face-centered lattice of isolated BX_6 octahedral units bridged by A-site cations in the void. Alternatively, the structure can be thought of as an ordered double perovskite of the formula $A_2B\square X_6$, with rock salt ordering of BX_6 and $\square X_6$ octahedra, where $\square$ denotes a vacancy, as shown in Figure 1. Anharmonicity in the vacancy-ordered double perovskites Cs_2SnI_6, $(CH_3NH_3)_2SnI_6$, and $(CH(NH_2)_2)_2SnI_6$ has been correlated with reduced carrier mobilities.[31] Replacing the inorganic Cs^+ with the molecular methylammonium ($CH_3NH_3{}^+$) and formamidinium ($CH(NH_2)_2{}^+$) cations is accompanied by a significant reduction in electron mobilities due to softer, more anharmonic lattice dynamics that result in stronger electron-phonon coupling interactions. In order to leverage anharmonicity as a design principle for perovskite halide semiconductors, a fundamental understanding of the structural and compositional origins of anharmonic lattice dynamics are required.

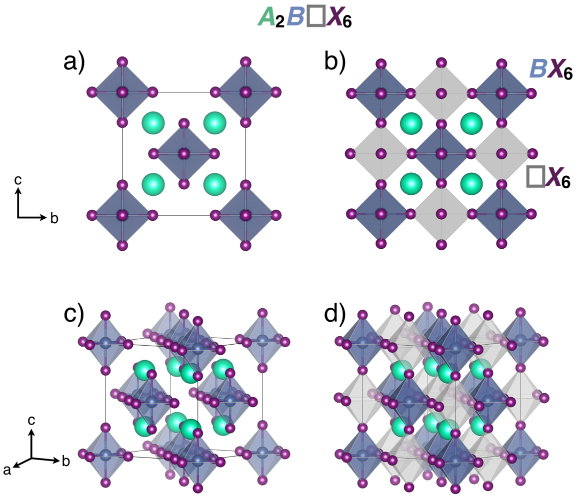

Fig. 1 Unit cell representation of the cubic vacancy-ordered double perovskite structure. A-site cations are shown in teal, B-site cations are shown in blue, and X-site anions are shown in purple. Panels (a) and (c) highlight the isolated BX_6 octahedral units. In (b) and (d), the grey, transparent octahedra represent the ordered vacancies, denoted as $\square X_6$.

In this contribution, we assess the structural origins of anharmonicity in the series of inorganic vacancy-ordered double perovskites $Cs_2Sn_{1-x}Te_xI_6$. X-ray pair distribution function analysis reveals asymmetry in the local coordination environment of Cs_2SnI_6, which systematically decreases and vanishes with increasing tellurium content. Neutron total scattering of Cs_2SnI_6 reveals that the peak asymmetry becomes increasingly pronounced at higher temperatures, indicating that this feature is likely due to a dynamic effect rather than a static structural distortion. We attribute the subtle deviations in the local coordination environment of the $Cs_2Sn_{1-x}Te_xI_6$ series to anharmonic lattice dynamics brought about by octahedral rotations and Cs^+ displacements, consistent with the concave-down shape of the atomic displacement parameter vs. temperature curves for cesium and iodine. This assertion is supported by pseudo-rigid-body Reverse Monte Carlo simulations of Cs_2SnI_6 and Cs_2TeI_6. From the RMC-optimized structures, we find that the Cs–I and I–I$_{\text{inter}}$ partial pair correlations exhibit a broad, asymmetric distribution, indicating that the anharmonicity arises from these atom pairs. We further quantified the trend in anharmonicity in the XPDFs of $Cs_2Sn_{1-x}Te_xI_6$ using a modified anharmonic Toda potential and find a strong correlation of the peak asymmetry with the calculated bond valence of the Cs^+ cation, suggesting that the anharmonicity arises due to dissatisfied bonding preferences of the Cs^+ cation within the cuboctahedral void, giving rise to dynamic octahedral rotations coupled to displacements of the Cs^+ ions. The relationship between bonding and anharmonicity provides a handhold for tuning the vibrational properties in vacancy-ordered double perovskite semiconductors.

Methods and Materials

Synthesis of $Cs_2Sn_{1-x}Te_xI_6$

The solid solution series $Cs_2Sn_{1-x}Te_xI_6$ was prepared by previously reported methods.[32]

Structural Characterization

Synchrotron X-ray scattering data suitable for pair distribution function (PDF) analysis were collected at beamline 11-ID-B at the Advanced Photon Source, Argonne National Laboratory, using 86 keV photons and sample-detector distance of 19 cm. Powdered samples of $Cs_2Sn_{1-x}Te_xI_6$ were loaded into polyimide capillaries and measured in transmission mode at room temperature using a PerkinElmer amorphous silicon image plate detector.[33] Experimental PDFs were extracted using PDFgetX3[34] and analyzed using PDFgui.[35] The program Fit2D[36] was used to calibrate the sample to detector distance and detector alignment with data from a CeO_2 powder standard. Raw scattering data were integrated into Q-space spectra, applying a mask and polarization correction during integration. The normalized total scattering pattern, $S(Q)$, was produced in PDFgetX3 by subtracting polyimide container scattering, utilizing the appropriate sample composition, and applying standard corrections for the area detector setup.[33] The pair distribution function pattern, $G(r)$, was calculated via Fourier transformation of the total scattering data utilizing a maximum $Q = 30$ Å^{-1}. $G(r)$ for each member of the series was extracted for several values of Q_{max} to infer the influence of Fourier termination ripples in our subsequent analyses. Values of $Q_{\text{damp}} = 0.0538$ Å^{-1} and $Q_{\text{broad}} = 0.003$ Å^{-1} were extracted from refinement of a Ni standard in PDFgui and used for further refinement.

Neutron total scattering measurements of Cs_2SnI_6 were performed on the Nanoscale Ordered Materials Diffractometer (NOMAD) at the Spallation Neutron Source, Oak Ridge National Laboratory. For measurements collected at T = 90, 300, and

500 K, a powdered sample of Cs_2SnI_6 was loaded and sealed in a quartz capillary (capillary diameter = 3.0 mm) in the multisample changer. Data were normalized against scattering data collected for an empty quartz capillary, and background scattering from the quartz capillary was subtracted. For measurements at $T = 10$ K, a powdered sample of Cs_2SnI_6 was loaded into a 6 mm vanadium canister under He atmosphere. Data were normalized against scattering collected for a vanadium rod, and background scattering from the vanadium can was subtracted.

Temperature-dependent neutron total scattering data were merged to the total scattering structure function using the IDL codes developed for the NOMAD instrument.[37] The pair distribution function was then produced through the sine Fourier transform of the total scattering structure function using $Q_{\text{max}} = 31.4$ Å^{-1}. For Cs_2SnI_6 at $T = 90$, 300, and 500 K, values of $Q_{\text{damp}} = 0.0201$ Å^{-1} and $Q_{\text{broad}} = 0.0196$ Å^{-1} were extracted from refinement of a diamond standard in PDFgui. For Cs_2SnI_6 at $T = 10$ K, values of $Q_{\text{damp}} = 0.01766$ Å^{-1} and $Q_{\text{broad}} = 0.01918$ Å^{-1} were extracted from refinement of a silicon standard. Analysis of the nPDFs was performed using PDFgui.

Reverse Monte Carlo simulations

Reverse Monte Carlo (RMC) simulations were performed with $6 \times 6 \times 6$ supercells of the cubic structures of Cs_2SnI_6 ($a = 69.830$ Å) and Cs_2TeI_6 ($a = 70.212$ Å), each containing 7,776 atoms. The simulations were constrained in reciprocal-space by $S(Q) - 1$ data, and in real-space by the X-ray pair distribution function, $G(r)$. $S(Q) - 1$ was convolved with a Gaussian function with a full-width-half-maximum of $^1/_2$ the length of the supercell edge prior to use in simulations in order to capture appropriate peak broadening due to finite size of the box.[38] The experimental data were simulated using two independent RMC approaches within the fullrmc package.[39] Both RMC simulations were run for 89,882,085 steps.

Traditional free-motion RMC simulations were performed in which all atoms were independently allowed to displace randomly within the Cartesian reference. The Sn–I/Te–I bond lengths were constrained between 2.65 Å$-$3.05 Å and the I–Sn–I and I–Te–I bond angles were constrained to 80-100° and 170-180°. The simulations were optimized against the experimental data from 0.9-17.45 Å for $G(r)$ and 0.5-0.25 Å^{-1} for $S(Q) - 1$.

Pseudo-rigid-body RMC simulations were also implemented, in which the $[SnI_6]$ and $[TeI_6]$ octahedra were randomly rotated and tilted as rigid units, prior to and after their free relaxation. Similarly to the free-motion RMC simulations, the Sn–I/Te–I bond lengths were constrained between 2.65 Å$-$3.05 Å and the I–Sn–I and I–Te–I bond angles were constrained to 80-100° and 170-180°. After initiating the refinements with only the intraoctahedron bonds, the refinement range was increased step-wise to include longer-range pair correlations while all atoms were permitted to displace in the Cartesian reference. After the fitting range reached $r = 17.45$ Å and after a finite number of atomic displacements, the octahedra were constrained as rigid bodies (Sn/Te–I bond lengths were frozen) and allowed to tilt about the center of the octahedra around all three Euler angles up to a maximum tilt angle of 10°. The entire fitting process was reiterated twice from the start to achieve the final configuration.

VESTA was used to visualize and render all crystal structures presented in this publication.[40]

Results

All members of the $Cs_2Sn_{1-x}Te_xI_6$ series crystallize in the cubic vacancy-ordered double perovskite structure shown in Figure 1.[32] The Sn(IV) and Te(IV) ions randomly occupy the *B*-site coordinated to six I^- ions at the *X*-site, and the Cs^+ cations occupy the cuboctahedral *A*-site void.

The local coordination environment probed by XPDF analysis is consistent with solid solution behavior between Cs_2SnI_6 and Cs_2TeI_6. In Figure 2a, the the X-ray pair distribution function (XPDF) of each member of the $Cs_2Sn_{1-x}Te_xI_6$ series are modeled with the cubic structural model with appropriate fractional occupancies of tin and tellurium. Over medium and long length scales ($r > 6$ Å), the XPDFs are fairly well described by the cubic structural model, consistent with each member of the series adopting the cubic vacancy-ordered double perovskite structure; however, the fit quality is worse closer to Cs_2SnI_6 (Figure 2b). As shown in Figure 3a, tellurium substitution is accommodated by a linear increase in the lattice parameter, consistent with Vegard's law. Further, the larger tellurium ion results in an increase in the average *B*–I bond length (Figure 3b) at the expense of the inter-octahedral I–I contact distances along the $\langle 110 \rangle$ directions (Figure 3c). This also results in a slight increase in the average Cs–I bond lengths across the series (Figure 3d). The structural parameters extracted from the XPDF fits in Figure 3 are plotted with the previously reported parameters from analysis of high-resolution synchrotron powder X-ray diffraction data.[32]

Although all members of the series appear to adopt nearly identical crystalline structures by both SXRD and XPDF, the local coordination environment over short length scales reveals subtle differences across the series. The first nearest-neighbor pair correlation at $r \sim 2.85$-2.9 Å due to Sn–I/Te–I bonds moves to higher *r* due to an increase in the average *B*–I bond length with substitution of the larger tellurium ion. Despite mixed Sn–I and Te–I bond lengths, this peak remains symmetric across the series and is well-described by the cubic structural model, consistent with regular, undistorted BX_6 octahedral units.

In contrast, deviations in the next-nearest-neighbor (*nnn*) pair correlation at $r \sim 4.1$ Å, due to I–I and Cs–I pairs, are observed across the series, manifesting as a slight asymmetry of the high-*r* side of the peak present in the difference curves in Figure 2. The apparent asymmetry is most pronounced in Cs_2SnI_6 and gradually decreases with increasing tellurium content, consistent with the nearly monotonic decrease in R_{wp} with x shown in Figure 2b. Our previous work found that the XPDFs of the intermediate members could be obtained by a linear combination of the XPDFs of the Cs_2SnI_6 and Cs_2TeI_6 end members,[32] indicating that this apparent asymmetry evolves smoothly as a function of tellurium content. As the BI_6 octahedra remain relatively undistorted and all members of the solid solution adopt nearly identical crystal structures by X-ray diffraction, we propose that this asymmetry may be due to anharmonic lattice dynamics rather than a static structural distortion.

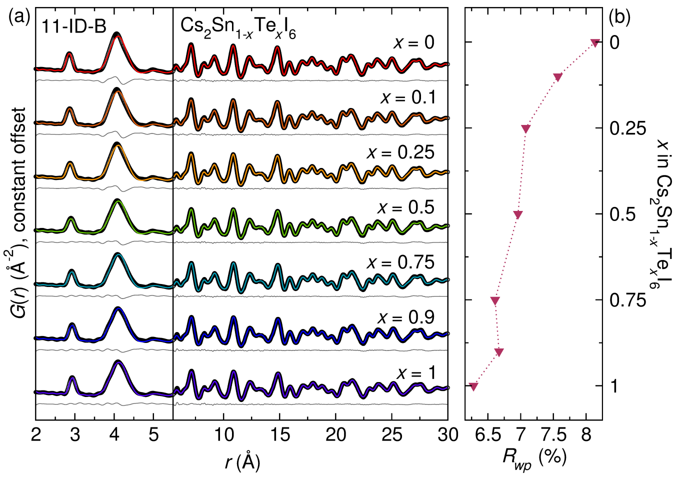

Fig. 2 (a) X-ray pair distribution functions of the solid solution Cs$_2$Sn$_{1-x}$Te$_x$I$_6$ modeled with the cubic vacancy-ordered double perovskite structure with isotropic, harmonic atomic displacement parameters. The data are shown as black circles, the fits are colored lines, and the difference is shown in grey. The x-axis is split to highlight the low-r pair correlations, particularly the asymmetry of the next-nearest neighbor pair correlation at $r \sim 4.1$ Å. The R_{wp} for each fit is shown in (b).

Neutron total scattering experiments of Cs$_2$SnI$_6$ reveal a temperature-dependence of the asymmetry observed in the local coordination environment. Neutron diffraction data of Cs$_2$SnI$_6$ collected from the 31° bank (bank 2) of NOMAD at T = 10, 90, 300, and 500 K reveal that Cs$_2$SnI$_6$ adopts the cubic vacancy-ordered double perovskite structure at all measured temperatures, as shown in the Rietveld refinements in Figure 4. The neutron pair distribution functions (nPDF) extracted from total scattering data are shown in Figure 5. At all temperatures the nPDFs were modeled with the cubic vacancy-ordered double perovskite structure of Cs$_2$SnI$_6$, consistent with previous reports[32,41] and with the corresponding diffraction data that indicates Cs$_2$SnI$_6$ adopts the cubic structure at all temperatures (Figure 4). At T = 10 K, the pair correlations are sharp, narrow, and symmetric, consistent with low-amplitude harmonic thermal vibrations at this temperature. Increasing temperature to T = 90 K and T = 300 K is accompanied by broadening of all pair correlations. The *nnn* pair correlation becomes visibly asymmetric with increasing temperature, with a slight tailing on the high-r side of the peak revealed in the difference curves. At T = 500 K, the peaks in the nPDF are significantly broadened and dampened, and we observe significant asymmetry of the *nnn* pair correlation that is not captured by the cubic structural model. The nPDFs for Cs$_2$SnI$_6$ at T = 10, 90, and T = 300 K are taken from our previous study and re-fit here for comparison with the T = 500 K data.[41]

Temperature-dependent peak asymmetries have been observed in the XPDF of the related perovskite CsSnBr$_3$.[42,43] At T = 300 K, the nearest-neighbor pair correlation due to Sn–Br bonds is symmetric, but becomes noticeably asymmetric on the high-r side of the peak at higher temperatures. The emergence of this asymmetry with temperature, termed "emphanisis", has been attributed to dynamic off-centering of the Sn^{2+} ion within the SnBr$_6$ octahedra, which arises from stereochemically-active 5s^2 electrons. While the formal [Kr]4d^{10}5s^0 electron configuration of Sn^{4+} in Cs$_2$SnI$_6$ precludes the presence of stereochemically-driven structural distortions, the temperature dependence of the peak asymmetry suggests that this effect arises from high-amplitude anharmonic lattice vibrations rather than a static structural distortion.

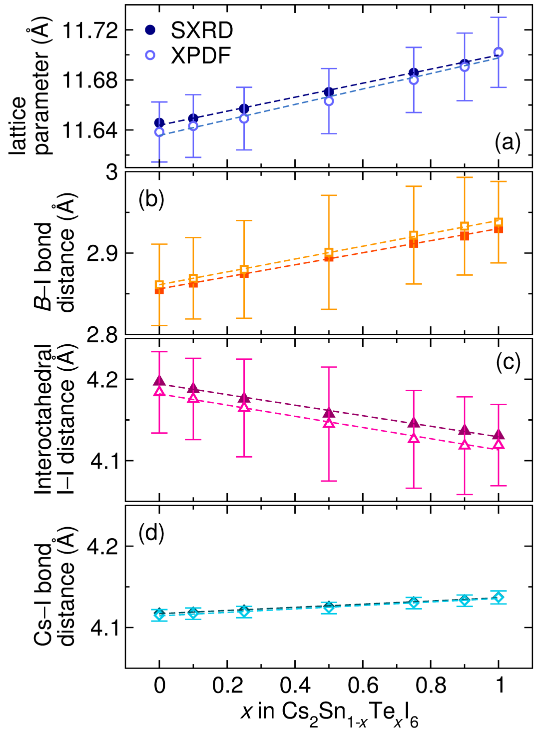

Fig. 3 Structural parameters for the Cs$_2$Sn$_{1-x}$Te$_x$I$_6$ solid solution from refinement of the cubic structural models against high-resolution synchrotron powder X-ray diffraction (SXRD) data (filled symbols) and X-ray pair distribution function analysis (open symbols). In (a), the lattice parameters for each member of the solid solution follow Vegard's law. In (b), the average B–I bond lengths increase linearly with substitution of the larger tellurium ion at the expense of the interoctahedral I–I contact distance along the $\langle 110 \rangle$ direction shown in (c). In (d), the average Cs–I bond length increases. The dashed lines represent linear regressions performed for each data set. Error bars are shown for the parameters extracted from the XPDF fits. The error bars for the SXRD parameters are within the size of the symbol and are therefore omitted for clarity. The structural parameters from the SXRD data are taken from Ref.[32].

To gain insight into the atomistic contributions to the anharmonicity and peak asymmetry in Cs$_2$SnI$_6$, we extracted values for the atomic displacement parameters (ADPs) from the Rietveld refinements of the neutron diffraction data shown in Figure 4. The iodine ADPs were refined anisotropically; U_{11} corresponds to displacements along the Sn–I bond, while $U_{22} = U_{33}$ corresponds to displacements perpendicular to the Sn–I bond. As shown in Figure 6, the ADPs for Cs and I ($U_{22} = U_{33}$) increase monotonically (though not linearly) with increasing temperature, while the ADPs for Sn and I (U_{11}) increase only slightly from T = 10 K to T = 500 K. In systems with harmonic interactions, the relationship between the atomic displacement parameter (U_{iso}) and temperature is well-described by a Debye-Waller model.[44,45] In Cs$_2$SnI$_6$, however, the ADPs for Cs and I $U_{22} = U_{33}$ follow a

This journal is © The Royal Society of Chemistry [year]

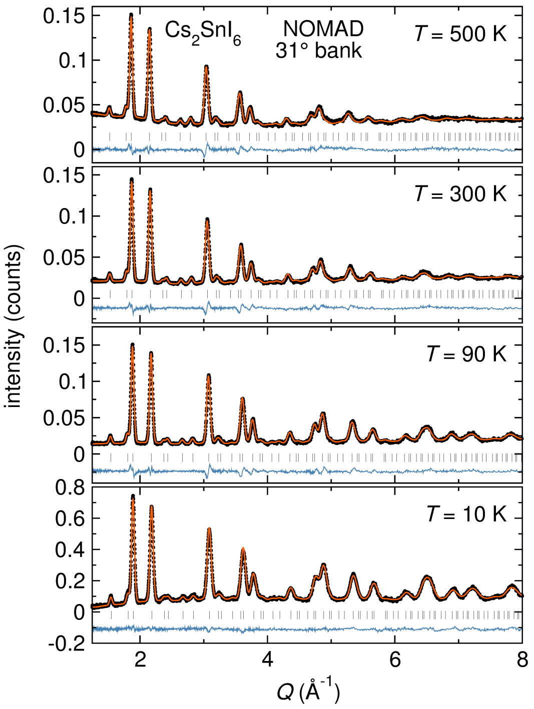

Fig. 4 Rietveld refinements of temperature-dependent neutron diffraction of Cs$_2$SnI$_6$ at T = 10, 90, 300, and T = 500 K from the 31° bank (bank 2) of the NOMAD instrument at the Spallation Neutron Source, Oak Ridge National Laboratory. The data are modeled with the cubic vacancy-ordered double perovskite structure at all temperatures. Black circles are the data, the orange line is the fit, the blue line is the difference, and the grey tick marks represent positions of anticipated reflections for the $Fm\bar{3}m$ vacancy-ordered double perovskite structure. The data at T = 10, 90, and T = 300 K have been previously reported.[41]

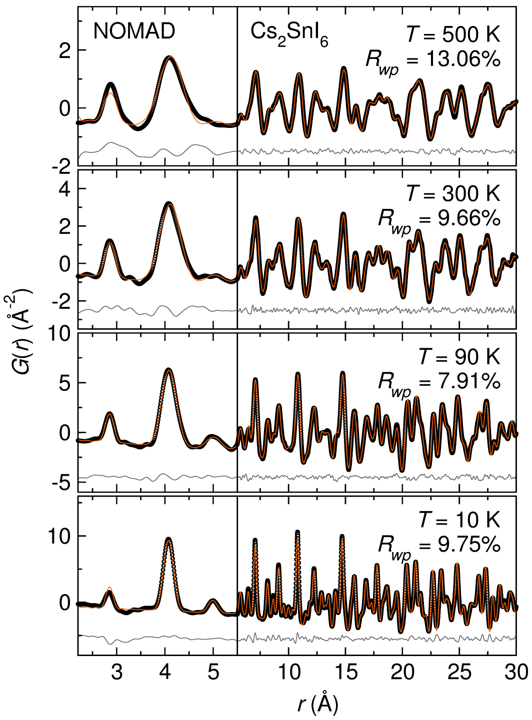

Fig. 5 Temperature-dependent neutron pair distribution function analysis of Cs$_2$SnI$_6$ at T = 10, 90, 300, and T = 500 K. The data are modeled with the cubic vacancy-ordered double perovskite structure at all temperatures. Black circles are the data, orange lines are the fits, and grey lines are the difference curves. The x-axis is split to highlight the low-r pair correlations and the increasing asymmetry of the next-nearest-neighbor pair correlation at $r \sim 4$ Å with increasing temperature. The nPDFs at T = 10, 90, and T = 300 K have been previously reported and are re-fit here for comparison with the T = 500 K data.[41]

concave-down shape with increasing temperature, a trend which has previously been attributed to anharmonic dynamics in the VAl$_{10+\delta}$ system due to rattling of the Al atoms within the structural voids.[45] Similarly, neutron diffraction studies of CsPbX_3 halide perovskites reveals anomalously large atomic displacement parameters of the Cs and X ions that diverge from the harmonic Debye-Waller model, indicating the presence of anharmonic effects due to coupled displacements of the Cs$^+$ and X^- ions.[46] The similarities observed between the VAl$_{10+\delta}$ and CsPbX_3 systems and Cs$_2$SnI$_6$ suggests that the trends in ADP vs. temperature arises from anharmonic dynamics of the Cs and I atoms in Cs$_2$SnI$_6$. Furthermore, the observation that iodine displacements perpendicular to the Sn–I bond ($U_{22} = U_{33}$) follow the same trend as the atomic displacement parameter for cesium and are significantly larger than iodine displacements along the Sn–I bond (U_{11}) may suggest the presence of [SnI$_6$] octahedral rotations coupled to Cs$^+$ displacements as the source of anharmonicity. Prior nuclear quadrupole resonance studies of the vacancy-ordered double perovskite family support this assertion, as dynamics in these materials originate predominantly from rotations of the rigid octahedral units.[47–50]

Reverse Monte Carlo (RMC) simulations of Cs$_2$SnI$_6$ and Cs$_2$TeI$_6$ were performed to provide atomistic insights into the asymmetry observed in the XPDFs. As the dominant lattice dynamics in vacancy-ordered double perovskites arise from octahedral rotations rather than deformations of the octahedra,[47–50] we elected to use a pseudo-rigid-body RMC approach, in which the isolated [SnI$_6$] and [TeI$_6$] octahedra were allowed to tilt as rigid bodies, to encourage chemically reasonable descriptions of the anharmonicity. The constraint of rigid-bodies has been shown to improve RMC simulation results, especially in cases with dynamics such as rigid-unit modes.[51] From this approach, we find that the XPDFs are best described by structures with random rotations of the SnI$_6$ and TeI$_6$ octahedra and displacements of the Cs$^+$ ions away from their crystallographic positions, as shown in the optimized supercells in Figure 7 and in the fits to the XPDF shown in Figure 8a and b. We have also performed traditional free-motion RMC simulations to ensure that the outcome is consistent with our pseudo-rigid-body RMC approach. These calculations are independently consistent with those of our pseudo-rigid-body approach, though the quality of fit is not as good for the same number of moves. These results are shown in the Supplemental Information.

To determine the atom pair contributions to the asymmetry observed in the next-nearest-neighbor pair correlation at $r \sim 4$ Å, the partial radial distribution functions (RDF) for the intraoctahedral I–I (I–I$_{\text{intra}}$), interoctahedral I–I (I–I$_{\text{inter}}$), and Cs–I pairs were extracted from the RMC-optimized supercells. As shown in

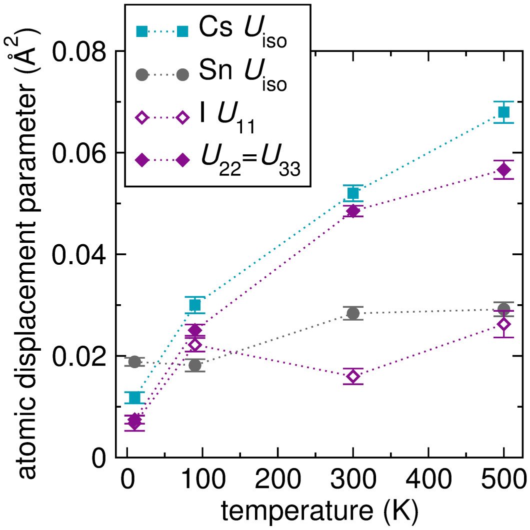

Fig. 6 Atomic displacement parameters (ADPs) extracted from the temperature-dependent neutron diffraction data for Cs_2SnI_6 using Rietveld analysis. Isotropic atomic displacement parameters were refined for cesium and tin. The ADPs for iodine were refined anisotropically, such that U_{11} corresponds to iodine displacements along the Sn–I bond and $U_{22} = U_{33}$ corresponds to displacements perpendicular to the Sn–I bond. The dotted lines are a guide to the eye to highlight the trends in ADP for each atom.

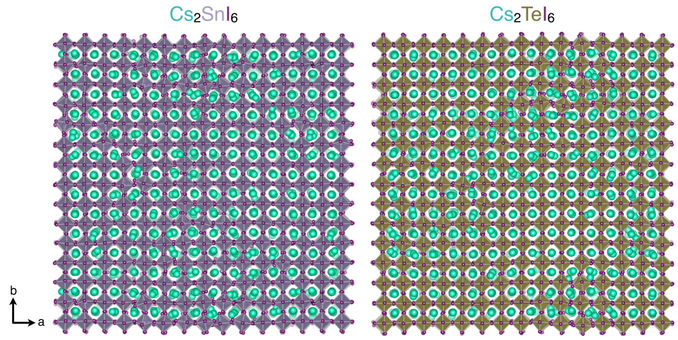

Fig. 7 Supercell structures of Cs_2SnI_6 and Cs_2TeI_6 optimized from pseudo-rigid-body RMC simulations.

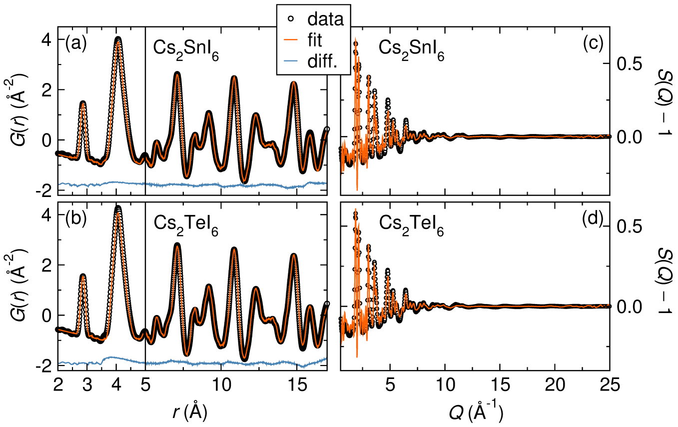

Fig. 8 Calculated $G(r)$ and $S(Q)-1$ from pseudo-rigid-body RMC-optimized supercells of Cs_2SnI_6 and Cs_2TeI_6 compared against the experimental $G(r)$ and $S(Q)-1$ from X-ray total scattering data. Experimental data are shown as open circles, the fits from the RMC optimizations are shown as orange lines, and the difference curves are shown as blue lines. The *x*-axes in (a) and (b) are split to highlight the low-*r* pair correlations.

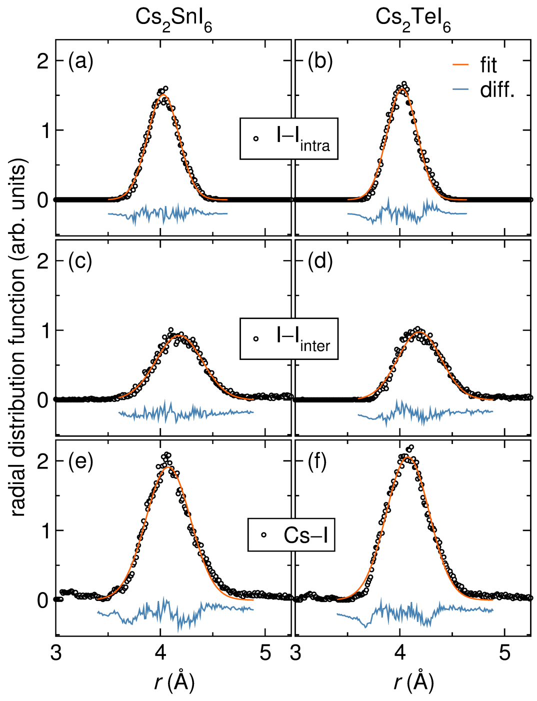

Fig. 9 Partial radial distribution functions for I–I$_{intra}$ (a,b), I–I$_{inter}$ (c,d), and Cs–I (e,f) pair correlations in Cs_2SnI_6 and Cs_2TeI_6 obtained from pseudo-rigid-body Reverse Monte Carlo simulations (circles). The distributions are fit with Gaussian functions, shown by the orange line. The difference curves are shown in blue and reveal asymmetries in the I–I$_{inter}$ and Cs–I RDFs.

Figure 9, the partial RDFs are relatively consistent between both Cs_2SnI_6 and Cs_2TeI_6 and show only subtle variations between the two compounds. In both compounds, the I–I$_{intra}$ RDFs for Cs_2SnI_6 and Cs_2TeI_6 are fairly well-described by a Gaussian function. In contrast, both the I–I$_{inter}$ and Cs–I partials exhibit an asymmetric peak shape evidenced by the deviations from a Gaussian function shown in Figure 9, indicating that the overall peak asymmetry arises due to these atom pairs. It is important to note that the I–I$_{inter}$ and Cs–I pairs in both Cs_2SnI_6 and Cs_2TeI_6 exhibit slightly asymmetric peak shapes, and therefore we cannot unambiguously assign one compound as being more anharmonic than the other from these simulations. Instead, these simulations are consistent with the notion that anharmonicity in these compounds arises from octahedral rotations coupled with displacements of the Cs^+ cations.

In order to quantify the trends in anharmonicity across the intermediate members of the $Cs_2Sn_{1-x}Te_xI_6$ series, the asymmetry of the *nnn* pair correlation was modeled with a modified Toda potential, which has been previously used to describe anharmonic interactions between nearest-neighbors in a linear atomic chain.[52,53] This modified Toda potential, $U(r)$, takes the form

$$U(r) = \frac{\mu}{\beta^2} e^{-\beta(r-b)} + \frac{\mu}{\beta}(r-b) - \frac{\mu}{\beta^2}, \tag{1}$$

where μ is the elastic constant, β is the degree of anharmonicity, and b is the interatomic distance. Harmonic interactions are described in the limit as $\beta \to 0$. The potential, $U(r)$, was approximated as the potential of mean force and then transformed to the reduced pair distribution function, $G(r)$, via $G(r) = [(k_B T e^{-U(r)})/r] - 4r\pi\rho_0$, where ρ_0 is the average number density, N/V, of each member of the series. The transformed Toda potential was fit to the asymmetric pair correlation at ~4.1 Å in the XPDF for each member of the $Cs_2Sn_{1-x}Te_xI_6$ series (Figure 10a) using a non-linear least squares optimizer implemented in Python. In Figure 10b and c, the fitted parameters for the interatomic distance (b) and the degree of anharmonicity (β) are plotted as a function of x in $Cs_2Sn_{1-x}Te_xI_6$. From this analysis, we find that the interatomic distance (b) increases linearly with increasing tellurium content, consistent with the increase in Cs–I bond length extracted from fits to the XPDF data shown in Figure 3d. Of particular significance is the trend in the degree of anharmonicity (Figure 10b), which decreases linearly with increasing tellurium content, consistent with qualitative inspection of the fits to the XPDFs shown in Figure 2. We note that the Toda potential is conventionally used to describe anharmonic interactions in a linear atomic chain, and thus our use of the Toda potential to describe the more complex interactions in this system serves as a comparative analysis of the trends in anharmonicity between members of the $Cs_2Sn_{1-x}Te_xI_6$ series.

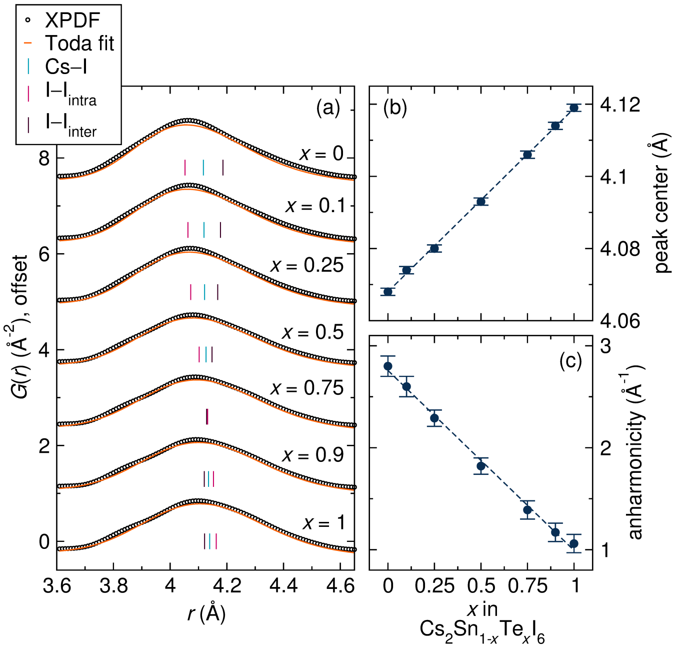

Fig. 10 (a) Toda potential fits to the next-nearest-neighbor pair correlation in the X-ray pair distribution function analysis for $Cs_2Sn_{1-x}Te_xI_6$. The data are shown as black circles and the fit is the orange line. The PDF data are fit with one Toda potential peak, and are offset vertically for comparison and clarity. In (b) and (c), the interatomic distance (b) and degree of anharmonicity (β) are plotted as a function of x in $Cs_2Sn_{1-x}Te_xI_6$, respectively. The colored tick marks in (a) represent the contact distances for Cs–I (teal), intraoctahedral I–I (pink), and interoctahedral I–I (purple) atom pairs taken from the refinements of the cubic model against the XPDF data from Figure 2. Dashed lines in (b) and (c) represent linear regressions.

Discussion

Previous studies of anharmonicity in perovskite halides provide further insight into the atomistic origins of anharmonicity in the inorganic vacancy-ordered double perovskites presented here. In our previous study of the series of vacancy-ordered double perovskites $(CH_3NH_3)_2SnI_6$ and $(CH(NH_2)_2)_2SnI_6$, we observed significant tailing of the A–I/I–I pair correlation of the XPDFs of the hybrid compounds. In the hybrid compounds, the extensive tailing observed in the XPDF was attributed to coupled organic-inorganic dynamics via hydrogen bonding interactions resulting in a distinctly anharmonic potential.[31] However, the lack of hydrogen bonding interactions available in Cs_2SnI_6, yet asymmetry in the local coordination environment, indicates that the anharmonicity originates from a different source.

We propose that the subtle deviations in the Cs–I/I–I pair correlations of the $Cs_2Sn_{1-x}Te_xI_6$ series arise from anharmonic lattice dynamics originating from $[BI_6]$ octahedral rotations coupled with displacements of the Cs^+ ions. Octahedral rotations in vacancy-ordered double perovskites have been studied at length by nuclear quadrupole resonance, which reveal that these modes are the dominant source of dynamics in these materials.[47–50] Furthermore, prior studies of inorganic perovskite halides $CsPbX_3$ and $CsSnX_3$ have shown that anharmonic lattice dynamics originate from cooperative tilting of the BX_6 octahedral units coupled with small displacements of the A-site cations within the cuboctahedral void.[17,18,54] In the present study, the presence of octahedral rotations coupled with Cs^+ displacements is supported by analysis of the neutron total scattering experiments of Cs_2SnI_6; the concave-down shape of the curves for the Cs atoms and the I $U_{22} = U_{33}$ atomic displacement parameters with increasing temperature follow a similar trend observed for localized vibrations associated with an ion rattling in a cage.[45] Notably, the iodine atomic displacement parameter parallel to the Sn–I bond (U_{11}) remains relatively constant while the perpendicular displacements ($U_{22} = U_{33}$) increase significantly with temperature. This observation indicates that iodine displacements perpendicular to the Sn–I bond dominate over those parallel to the Sn–I bond, lending further support to the notion of octahedral tilting as the primary source of dynamics and anharmonicity in Cs_2SnI_6.

Table 1 Bond valence sum analysis for Cs–I bonds in $Cs_2Sn_{1-x}Te_xI_6$. Cs–I bond lengths were taken from the XPDF and SXRD analyses. Values of B = 0.609 and R_0 = 2.6926 Å were used in calculation of the bond valence sum.[55]

	XPDF		SXRD	
x	Cs–I length (Å)	BVS	Cs–I length (Å)	BVS
0	4.115	1.161	4.118	1.156
0.1	4.117	1.158	4.119	1.154
0.25	4.119	1.154	4.122	1.149
0.5	4.124	1.145	4.126	1.140
0.75	4.130	1.134	4.132	1.130
0.9	4.133	1.127	4.134	1.125
1	4.137	1.119	4.137	1.119

Anharmonicity in the vacancy-ordered double perovskites $Cs_2Sn_{1-x}Te_xI_6$ can be correlated with the bonding preferences of

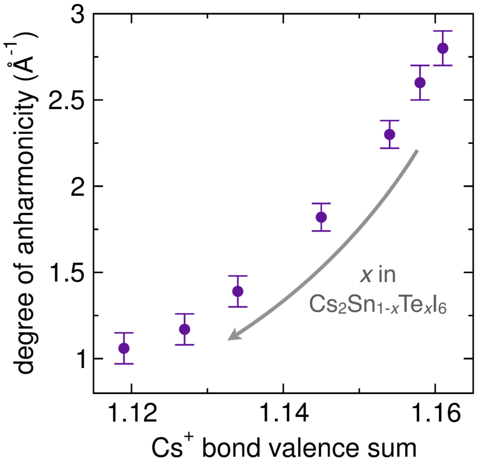

Fig. 11 The degree of anharmonicity from the Toda potential fits plotted as a function of the Cs^{+} bond valence sum derived from XPDF analysis.

the cesium cation within the cuboctahedral void. In Figure 11, the degree of anharmonicity extracted from the Toda potential fits are plotted as a function of the Cs^{+} bond valence sum. For $x = 1$ (Cs_2TeI_6), the degree of anharmonicity is the lowest and corresponds with a bond valence sum of ∼1.12, suggesting that the Cs^{+} is most optimally bonded in Cs_2TeI_6. As tellurium is replaced with tin, the bond valence sum of Cs^{+} increases concomitantly with an increase in the degree of anharmonicity, reaching a maximum bond valence of ∼1.16 for Cs_2SnI_6. This analysis suggests that the anharmonicity is minimized when the size of the cuboctahedral void satisfies the bonding preferences of the Cs^{+} cation. Conversely, increasingly anharmonic lattice dynamics are therefore expected as the bond valence of the Cs^{+} ion diverges from ideal coordination.

The bond valence sum has previously been applied to other perovskite halide systems to predict the presence of dynamic and cooperative octahedral tilting distortions.[41,54,56,57] Bond valence sum calculations of the vacancy-ordered double perovskite Rb_2SnI_6 indicate that the coordination to the smaller Rb^{+} ion is optimized by symmetry-lowering cooperative octahedral tilting distortions,[41] as is also observed in the $Cs_{1-x}Rb_xPbX_3$ (X = Cl^{-}, Br^{-}) series.[57] In the $Cs_2Sn_{1-x}Te_xI_6$ series, the Cs^{+} coordination is nearly optimal in the cubic structural models, consistent with the observation that neither Cs_2SnI_6 nor Cs_2TeI_6 undergo structural phase transitions down to T = 10 K.[32] Rather, the slight deviations in bond valence sum in this system manifest as a small degree of anharmonicity. Therefore, anharmonic effects in vacancy-ordered double perovskites may be expected when the bond valence sum of the A-site cation deviates slightly from ideal, while more significant structural changes due to cooperative octahedral tilting may be expected if the A-site is significantly underbonded. As the properties of halide perovskites are intimately linked to (anharmonic) lattice dynamics, the bond valence sum provides a simple tool for predicting the presence and extent of anharmonic behavior and may further be leveraged as a design principle for materials with desired structure-dynamic-property relationships.

Conclusion

The series of vacancy-ordered double perovskites $Cs_2Sn_{1-x}Te_xI_6$ presents an interesting test case for anharmonic lattice dynamics. While each member of the series adopts the cubic vacancy-ordered double perovskite structure by high-resolution powder X-ray diffraction, the local coordination environment probed by X-ray pair distribution function analysis reveals subtle deviations. These deviations manifest as an emergent asymmetry of the next-nearest-neighbor pair correlation due to Cs–I and I–I atom pairs in Cs_2SnI_6, which gradually disappear with increasing tellurium content. Through analysis of temperature-dependent neutron pair distribution function analysis for Cs_2SnI_6, we propose that this asymmetry arises due to anharmonic lattice dynamics associated with coupled motions between the isolated SnI_6 octahedra and the Cs^{+} ions within the cuboctahedral void, supported by RMC simulations and the trends in atomic displacement parameters for the Cs and I atoms extracted from neutron diffraction data. Using bond valence sum analysis, we find that the valence for Cs^{+} is optimized when tellurium occupies the B-site rather than tin. This observation is consistent with the trends in anharmonicity extracted from Toda potential fits, and suggests that the asymmetry observed in the Cs–I/I–I pair correlation in the XPDFs of Sn-rich samples originates from dissatisfied bonding preferences of the Cs^{+} cation with the surrounding iodide cage. We further demonstrate that bond valence sum analysis can be correlated with anharmonic behavior in halide perovskites and used as a simple tool for predicting anharmonicity in perovskite halide systems.

Conflicts of interest

There are no conflicts to declare.

Acknowledgements

This work was supported by Grant DE-SC0016083 funded by the U.S. Department of Energy, Office of Science. J.R.N. and A.E.M. acknowledge support from Research Corporation for Science Advancement through a Cottrell Scholar Award, and J.R.N. thanks the A.P. Sloan Foundation for assistance provided from a Sloan Research Fellowship. Use of the Advanced Photon Source at Argonne National Laboratory was supported by the U.S. Department of Energy, Office of Science, Office of Basic Energy Sciences, under Contract No. DE-AC02-06CH11357. A portion of this research at ORNL's Spallation Neutron Source was sponsored by the Scientific User Facilities Division, Office of Basic Energy Sciences, U.S. Department of Energy. The authors thank Dr. K. Page, Dr. D. Olds, and Dr. T.-M. Usher from the NOMAD instrument at the Spallation Neutron Source, Oak Ridge National Laboratory and Dr. J. A. Kurzman and Dr. A. J. Martinolich for collection of X-ray total scattering data. The authors also thank the expert beamline scientists at 11-ID-B at the Advanced Photon Source, Argonne National Laboratory.

Notes and references

1 J. Dugdale and D. MacDonald, *Phys. Rev.*, 1955, **98**, 1751.

2 T. M. Brenner, D. A. Egger, A. M. Rappe, L. Kronik, G. Hodes and D. Cahen, *J. Phys. Chem. Lett.*, 2015, **6**, 4754–4757.

3 S. Muy, J. C. Bachman, L. Giordano, H.-H. Chang, D. L. Abernathy, D. Bansal, O. Delaire, S. Hori, R. Kanno, F. Maglia, S. Lupart, P. Lamp and Y. Shao-Horn, *Energ. Environ. Sci.*, 2018, **11**, 850–859.

4 S. Chodos, A. Black and C. Flint, *J. Chem. Phys.*, 1976, **65**, 4816–4824.

5 V. Hizhnyakov, V. Plekhanov, V. Shepelev and G. Zavt, *Phys. Status Solidi B*, 1981, **108**, 531–540.

6 J. Freire and R. Katiyar, *Phys. Rev. B*, 1988, **37**, 2074.

7 D. Khatib, R. Migoni, G. Kugel and L. Godefroy, *J. Phys.: Condens. Matter*, 1989, **1**, 9811.

8 J. Bardeen, L. N. Cooper and J. R. Schrieffer, *Phys. Rev.*, 1957, **106**, 162.

9 Z. Dughaish, *Physica B: Condens. Matter*, 2002, **322**, 205–223.

10 B. Sangiorgio, E. S. Bozin, C. D. Malliakas, M. Fechner, A. Simonov, M. G. Kanatzidis, S. J. Billinge, N. A. Spaldin and T. Weber, *arXiv preprint arXiv:1709.02863*, 2017.

11 L.-D. Zhao, S.-H. Lo, Y. Zhang, H. Sun, G. Tan, C. Uher, C. Wolverton, V. P. Dravid and M. G. Kanatzidis, *Nature*, 2014, **508**, 373.

12 X. Shi, J. Yang, J. R. Salvador, M. Chi, J. Y. Cho, H. Wang, S. Bai, J. Yang, W. Zhang and L. Chen, *J. Am. Chem. Soc.*, 2011, **133**, 7837–7846.

13 R. Cava, F. Reidinger and B. Wuensch, *Solid State Ionics*, 1981, **5**, 501–504.

14 A. Yoshiasa, K. Koto, F. Kanamaru, S. Emura and H. Horiuchi, *Acta Crystallogr. B*, 1987, **43**, 434–440.

15 X.-Y. Zhu and V. Podzorov, *J. Phys. Chem. Lett.*, 2015, **6**, 4758–4761.

16 C. E. Patrick, K. W. Jacobsen and K. S. Thygesen, *Phys. Rev. B*, 2015, **92**, 201205.

17 O. Yaffe, Y. Guo, L. Z. Tan, D. A. Egger, T. Hull, C. C. Stoumpos, F. Zheng, T. F. Heinz, L. Kronik, M. G. Kanatzidis, J. S. Owen, A. M. Rappe, M. A. Pimenta and L. E. Brus, *Phys. Rev. Lett.*, 2017, **118**, 136001.

18 R. X. Yang, J. M. Skelton, L. da Silva, J. M. Frost and A. Walsh, *J. Phys. Chem. Lett.*, 2017, **8**, 4720–4726.

19 A. N. Beecher, O. E. Semonin, J. M. Skelton, J. M. Frost, M. W. Terban, H. Zhai, A. Alatas, J. S. Owen, A. Walsh and S. J. Billinge, *ACS Energy Lett.*, 2016, **1**, 880–887.

20 M. M. Lee, J. Teuscher, T. Miyasaka, T. N. Murakami and H. J. Snaith, *Science*, 2012, **338**, 643–647.

21 S. D. Stranks and H. J. Snaith, *Nat. Nanotechnol.*, 2015, **10**, 391–402.

22 D. Shi, V. Adinolfi, R. Comin, M. Yuan, A. Alarousu, Erkki andd Rothen Buin, Y. Chen, A. Hoogland, Sjoerd anberger, K. Katsiev, Y. Losovy, X. Zhang, P. A. Dowben, O. F. Mohammed, E. H. Sargent and O. M. Bakr, *Science*, 2015, **347**, 519–522.

23 Y. Bi, E. M. Hutter, Y. Fang, Q. Dong, J. Huang and T. J. Savenije, *J. Phys. Chem. Lett.*, 2016, **7**, 923–928.

24 H. Zhu, K. Miyata, Y. Fu, J. Wang, P. P. Joshi, D. Niesner, K. W. Williams, S. Jin and X.-Y. Zhu, *Science*, 2016, **353**, 1409–1413.

25 M. Sendner, P. K. Nayak, D. A. Egger, S. Beck, C. Müller, B. Epding, W. Kowalsky, L. Kronik, H. J. Snaith, A. Pucci and R. Lovrincic, *Mater. Horiz.*, 2016, **3**, 613–620.

26 A. J. Neukirch, W. Nie, J.-C. Blancon, K. Appavoo, H. Tsai, M. Y. Sfeir, C. Katan, L. Pedesseau, J. Even, J. J. Crochet, G. Gupta, A. D. Mohite and S. Tretiak, *Nano Lett.*, 2016, **16**, 3809–3816.

27 A. Pecchia, D. Gentilini, D. Rossi, M. Auf der Maur and A. Di Carlo, *Nano Lett.*, 2016, **16**, 988–992.

28 M. Bonn, K. Miyata, E. Hendry and X.-Y. Zhu, *ACS Energy Lett.*, 2017, **2**, 2555–2562.

29 H. Zhu, M. T. Trinh, J. Wang, Y. Fu, P. P. Joshi, K. Miyata, S. Jin and X.-Y. Zhu, *Adv. Mater.*, 2017, **29**, 1–6.

30 C. Katan, A. D. Mohite and J. Even, *Nat. Mater.*, 2018, **17**, 377.

31 A. E. Maughan, A. M. Ganose, A. M. Candia, J. T. Granger, D. O. Scanlon and J. R. Neilson, *Chem. Mater.*, 2018, **30**, 472—483.

32 A. E. Maughan, A. M. Ganose, M. M. Bordelon, E. M. Miller, D. O. Scanlon and J. R. Neilson, *J. Am. Chem. Soc.*, 2016, **138**, 8453–8464.

33 P. J. Chupas, X. Qiu, J. C. Hanson, P. L. Lee, C. P. Grey and S. J. Billinge, *J. Appl. Crystallogr.*, 2003, **36**, 1342–1347.

34 P. Juhas, T. Davis, C. L. Farrow and S. J. Billinge, *J. Appl. Crystallogr.*, 2013, **46**, 560–566.

35 C. Farrow, P. Juhas, J. Liu, D. Bryndin, E. Božin, J. Bloch, T. Proffen and S. Billinge, *J. Phys.: Condens. Matter*, 2007, **19**, 335219.

36 A. Hammersley, S. Svensson, M. Hanfland, A. Fitch and D. Hausermann, *International Journal of High Pressure Research*, 1996, **14**, 235–248.

37 J. Neuefeind, M. Feygenson, J. Carruth, R. Hoffmann and K. K. Chipley, *Nucl. Instrum. Methods, Phys. Res. Sect. B*, 2012, **287**, 68–75.

38 M. G. Tucker, M. T. Dove and D. A. Keen, *J. Appl. Crystallogr.*, 2001, **34**, 630–638.

39 B. Aoun, *J. Comput. Chem.*, 2016, **37**, 1102–1111.

40 K. Momma and F. Izumi, *J. Appl. Crystallogr.*, 2011, **44**, 1272–1276.

41 A. E. Maughan, A. M. Ganose, M. A. Almaker, D. O. Scanlon and J. R. Neilson, *Chem. Mater.*, 2018, **30**, 3909—3919.

42 D. H. Fabini, G. Laurita, J. S. Bechtel, C. C. Stoumpos, H. A. Evans, A. G. Kontos, Y. S. Raptis, P. Falaras, A. Van der Ven, M. G. Kanatzidis and R. Seshadri, *J. Am. Chem. Soc.*, 2016, **138**, 11820–11832.

43 G. Laurita, D. H. Fabini, C. C. Stoumpos, M. G. Kanatzidis and R. Seshadri, *Chem. Sci.*, 2017, **8**, 5628–5635.

44 A. Lawson, J. Goldstone, B. Cort, R. Sheldon and E. Foltyn, *J. Alloys Compd.*, 1994, **213**, 426–428.

45 D. Safarik, T. Klimczuk, A. Llobet, D. Byler, J. Lashley, J. O'Brien and N. Dilley, *Phys. Rev. B*, 2012, **85**, 014103.

46 M. Sakata, J. Harada, M. Cooper and K. Rouse, *Acta Crystal-*

logr. A, 1980, **36**, 7–15.
47 G. O'Leary and R. Wheeler, *Phys. Rev. B*, 1970, **1**, 4409.
48 D. F. Cooke and R. L. Armstrong, *Can. J. Phys.*, 1971, **49**, 2381–2388.
49 R. L. Armstrong and K. R. Jeffrey, *Can. J. Phys.*, 1971, **49**, 49–53.
50 H. M. van Driel, R. L. Armstrong and M. M. McEnnan, *Phys. Rev. B*, 1975, **12**, 488.
51 M. J. Conterio, A. L. Goodwin, M. G. Tucker, D. A. Keen, M. T. Dove, L. Peters and J. S. Evans, *J. Phys. Condens. Matter*, 2008, **20**, 255225.
52 M. Toda, *J. Phys. Soc. Jpn.*, 1965, **20**, 2095A–2095A.
53 A. Milchev and G. Mazzucchelli, *Phys. Rev. B*, 1988, **38**, 2808.
54 J. S. Bechtel and A. Van der Ven, *Phys. Rev. Mater.*, 2018, **2**, 025401.
55 S. Adams, *Acta Crystallogr. B*, 2001, **57**, 278–287.
56 J. Young and J. M. Rondinelli, *J. Phys. Chem. Lett.*, 2016, **7**, 918–922.
57 M. R. Linaburg, E. T. McClure, J. D. Majher and P. M. Woodward, *Chem. Mater.*, 2017, **29**, 3507–3514.

This journal is © The Royal Society of Chemistry [year]

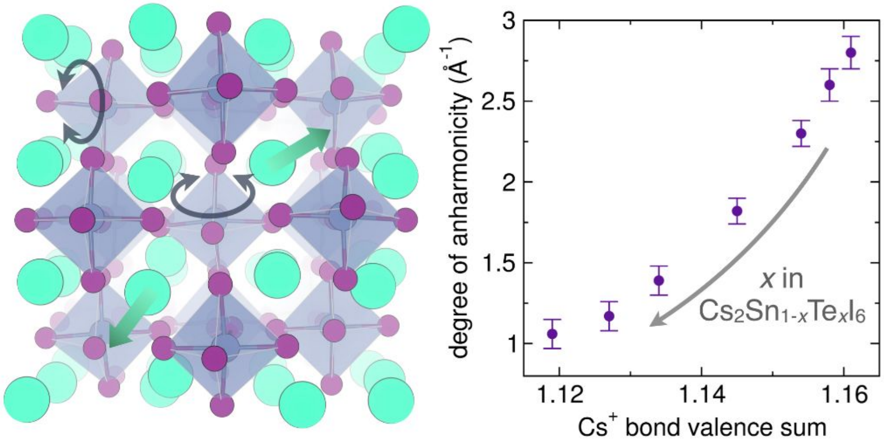

Anharmonicity is observed in vacancy-ordered double perovskites when the *A*-site cation is not optimally coordinated by the octahedral framework.